An electronic quantum eraser

E. Weisz *et al.*

Science **344**, 1363 (2014);
DOI: 10.1126/science.1248459

Science (print ISSN 0036-8075; online ISSN 1095-9203) is published weekly, except the last week in December, by the American Association for the Advancement of Science, 1200 New York Avenue NW, Washington, DC 20005.

41. Y. Rak *et al.*, *Am. J. Phys. Anthropol.* **144**, 247 (2011).
42. I. Tattersall, in *Continuity and Discontinuity in the Peopling of Europe: One Hundred Fifty Years of Neanderthal Study*, S. Condemi, G.-C. Weniger, Eds. (Springer Science+Business Media B.V., New York, 2011), chap. 4.
43. M. Meyer *et al.*, *Nature* **505**, 403–406 (2014).
44. M. Meyer *et al.*, *Science* **338**, 222–226 (2012).
45. L. J. Arnold *et al.*, *J. Hum. Evol.* **67**, 85–107 (2014).

ACKNOWLEDGMENTS

We are grateful to the Atapuerca team, especially A. Esquivel for work in SH and M. C. Ortega for restoration of the SH fossils, and to K. Ludwig, J. Rofes, and J. M. López-García for constructive discussions. E. Santos assisted with computed tomography scanning and J. Trueba provided the photos. For access to the comparative materials, we thank P. Mennecier, A. Froment, H. de Lumley, D. Grimaud-Hervé, C. B. Stringer, R. Kruszynski, G. D. Koufous, D. Mania, D. Lieberman, and J. Haas. A.G.-T. has a contract from the Ramón y Cajal Program (RYC-2010-06152). R.M.Q. received financial support from BU-SUNY and the AMNH. A.P.-P. has a MECD grant (AP-2009-4096). E.P.-R. has a CAM grant (S2010/BMD-2330). A.A.V. has a MINECO grant (BES-2010-039961). A.G.-O. and M.D. have a Marie Curie–IEF and a Marie Curie–IRG (PIRG8-GA-2010-276810) contracts. N.S., A.B., L.R., A.P.-P., A.A.V., and R.G. received Fundación Atapuerca grants. L.J.A. has an ARCFF grant (FT130100195). Dating at the Berkeley Geochronology Center was supported by the Ann and Gordon Getty Foundation. U-Th isotopic analysis at the HISPEC was supported by Taiwan ROC MOST and NTU grants (100-2116-M-002-009, 101-2116-M-002-009, 101R7625). Thanks to SGIker-UPV/EHU for their research facilities. This research was supported by the MINECO (CGL2012-38434-C03-01 and 03) and the JCyL (BU005A09, DGR 2009 SGR-324) projects. Fieldwork was funded by the JCyL and the Fundación Atapuerca. Junta de Castilla y León is the repository of the fossils.

SUPPLEMENTARY MATERIALS

www.sciencemag.org/content/344/6190/1358/suppl/DC1
Materials and Methods
Supplementary Text S1 to S9
Figs. S1 to S39
Tables S1 to S15
References (*46*–*178*)

26 March 2014; accepted 12 May 2014
10.1126/science.1253958

REPORTS

QUANTUM MECHANICS

An electronic quantum eraser

E. Weisz,* H. K. Choi,* I. Sivan, M. Heiblum,† Y. Gefen, D. Mahalu, V. Umansky

The quantum eraser is a device that illustrates the quantum principle of complementarity and shows how a dephased system can regain its lost quantum behavior by erasing the "which-path" information already obtained about it. Thus far, quantum erasers were constructed predominantly in optical systems. Here, we present a realization of a quantum eraser in a mesoscopic electronic device. The use of interacting electrons, instead of noninteracting photons, allows control over the extracted information and a smooth variation of the degree of quantum erasure. The demonstrated system can serve as a first step toward a variety of more complex setups.

Complementarity in quantum measurements is a core concept of quantum mechanics (*1*), closely related to Heisenberg's uncertainty principle, although the exact relation between the two remains a source of debate (*2*–*8*). An example of complementarity is the double-slit interference experiment: If we measure a particle's position, the measurement will quench its wavelike nature; vice versa, observing the wave behavior via interference implies lack of knowledge of the particle's path. A canonical system for exploring complementarity is the quantum eraser, predominantly studied in photonic systems (*9*–*16*). A quantum eraser is an interference experiment consisting of two stages. First, one of the interfering paths is coupled to a "which-path" detector, resulting in loss of interference due to acquisition of which-path information. Second, the which-path information is being "erased" by projecting the detector's wave function on an adequately chosen basis; this renders the which-path information inaccessible, which allows reconstruction of the interference pattern.

Here, we present an implementation of a quantum eraser in an electronic system. Our system consists of two identical electronic Mach-Zehnder interferometers (MZIs) (*17*) entangled via Coulomb interactions. Initially proposed by Kang (*18*) and studied theoretically in (*19*, *20*), this setup consists of two MZI: one serving as a path detector and the other as the system interferometer, where the visibility of the Aharonov-Bohm (AB) oscillation in the system can be controlled by the detector (*21*–*23*).

An electronic MZI is formed by manipulating quasi–one-dimensional, chiral edge channels, which are formed in the integer quantum Hall effect regime (*17*). Potential barriers, formed by quantum point contacts (QPCs), take the role of optical beam splitters, transmitting and reflecting impinging electrons with amplitudes t_i and r_i, respectively, where $|t_i|^2 + |r_i|^2 = 1$ and $t_i, r_i \in R$. Two such coupled MZIs are shown in Fig. 1, where the coupling is mediated by the lower path of the system and the upper path of the detector, referred to as interacting paths (shaded area in Fig. 1A).

Starting with the system, an electron injected from source S1 arrives at SQPC1 and is put into a superposition of being reflected into the interacting path and transmitted into the noninteracting path, namely, $|S\rangle = r_1|\uparrow\rangle_S + t_1|\downarrow\rangle_S$, with $|\uparrow\rangle_S$ and $|\downarrow\rangle_S$ standing for the interacting and noninteracting paths of the system, respectively. The paths recombine and interfere at SQPC2, with the electron's probability of reaching the drain D2 being $P(\mathrm{D2}) = |r_1 r_2 e^{i\phi_S} - t_1 t_2|^2 = T_0 - T_1\cos(\phi_S)$, where $T_0 \equiv |t_1 t_2|^2 + |r_1 r_2|^2$, $T_1 \equiv 2t_1 t_2 r_1 r_2$, $\phi_S = 2\pi AB/\Phi_0$ is the AB phase (*24*), $\Phi_0 = h/e$ is the magnetic flux quantum, A the area enclosed by the two paths, and B the magnetic field. The visibility of the interfering pattern at D2 is defined as $v_{\mathrm{D2}} \equiv \frac{\max[P(\mathrm{D2})] - \min[P(\mathrm{D2})]}{\max[P(\mathrm{D2})] + \min[P(\mathrm{D2})]} = \frac{T_1}{T_0}$. Throughout our experiments, all the QPCs were tuned to have equal transmission and reflection amplitudes, $|r_i|^2 = |t_i|^2 = \frac{1}{2}$; $i = 1...4$.

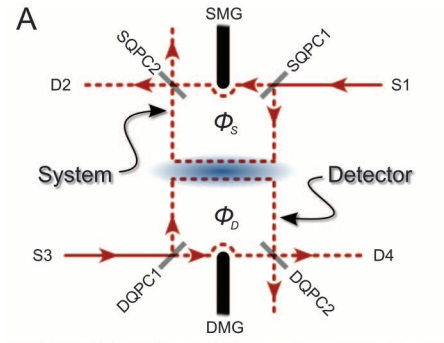

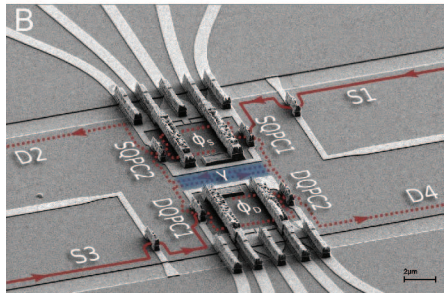

Fig. 1. Schematics and micrograph of the device under study. (**A**) The electronic quantum eraser consists of two identical electronic Mach-Zehnder interferometers (MZIs) entangled via Coulomb interactions. Quantum point contacts (QPCs) serve as beam splitters (full lines represent full beams, and dashed lines partitioned beams). (**B**) A scanning electron microscope micrograph of the fabricated structure, which was realized in a GaAs-AlGaAs heterostructure harboring a high-mobility two-dimensional electron gas. The edge channels were manipulated by biasing surface gates (bright gray) and surface etching. Ohmic contacts serve as sources (S1, S3) and drains (D2, D4), which allow electric access to the electron gas lying underneath the surface. The nanostructures were defined using electron-beam lithography.

Braun Center for Submicron Research, Department of Condensed Matter Physics, Weizmann Institute of Science, Rehovot 76100, Israel.
*These authors contributed equally to this work. **†Corresponding author. E-mail: moty.heiblum@weizmann.ac.il**

The Coulomb interaction between two electrons passing simultaneously in the interacting paths causes a slight mutual repulsion, which affects their trajectories and reduces the AB area in each MZI by δA_γ, which therefore adds a phase shift $\gamma = \delta A_\gamma B/\Phi_0$ (*25*). The closer the interacting edges, the larger the phase shift. The states of the detector are $|0\rangle_D = \frac{1}{\sqrt{2}}\,(e^{i\phi_D}|\uparrow\rangle_D + |\downarrow\rangle_D)$, if the system's electron passes through the noninteracting path, and $|\gamma\rangle_D = \frac{1}{\sqrt{2}}(e^{i(\phi_D+\gamma)}|\uparrow\rangle_D + |\downarrow\rangle_D)$, if it passes through the interacting path. The system-detector complex is thus in an entangled state $|\Psi\rangle = \frac{1}{\sqrt{2}}(|\downarrow\rangle_S|0\rangle_D + e^{i\phi_S}|\uparrow\rangle_S|\gamma\rangle_D)$, where the detector's state provides which-path information about the system. Consequently, the system is dephased, as is evident from its transmission probability $P(\mathrm{D2}) = \frac{1}{2} - \frac{1}{2}\mathrm{Re}(e^{i\phi_S}\langle 0|\gamma\rangle_D) = \frac{1}{2} - \frac{1}{4}[\cos(\phi_S) + \cos(\phi_S + \gamma)]$. This can be understood as the average of two interference patterns of the system: one with the unperturbed AB phase and one with the added interaction phase γ (Fig. 2, inset). An equivalent view (*26*) stems from the realization that the detector's interacting path carries shot noise (because of the current partitioning by DQPC1), which leads to an at least partial dephasing of the system.

The visibility of the system, an indicator of its coherence, is determined by the overlap of the detector states, $\langle 0|\gamma\rangle_D$: $v_{\mathrm{D2}} = |\langle 0|\gamma\rangle_D| = \cos(\gamma/2)$. In reality, the visibility of the system, without the presence of a detector, is limited because of uncontrolled dephasing from the external environment. Thus, the measured visibility of the system is

$$v_{\mathrm{D2}} = \xi\cos(\gamma/2) \qquad (1)$$

where $0 \le \xi \le 1$.

The detector states' distinguishability (D), its efficacy in acquiring the which-path information, is complementary to the system's interference visibility, namely, $D^2 + {v_{\mathrm{D2}}}^2 = 1$ (*27*–*29*), hence $D = \sin(\gamma/2)$in the ideal case $\xi = 1$; in other words, having the particle's which-path information, encoded in the detector's phase, comes at the expense of observing the particle's wavelike nature.

One can define the knowledge (K), the which-path information measured in our detector at drain D4, as

$$K(\phi_D) \equiv |P(\mathrm{D4}|\uparrow_S) - P(\mathrm{D4}|\downarrow_S)| = |D\,\sin(\phi_D + \frac{\gamma}{2})|, \qquad (2)$$

namely, the difference in the detector's output currents, for a certain AB phase ϕ_D, when the system's electron takes either of the possible paths. Whereas the distinguishability D indicates the which-path information encoded in the detector state, the knowledge K indicates how much of it is actually accessible. Naturally, the knowledge is bound by the distinguishability, $K \le D$. The knowledge K can be continuously tuned by altering the detector's AB phase ϕ_D between gaining full which-path information ($K = D$) and fully erasing it ($K = 0$).

Erasing the which-path information to allow recovery of the electron's wavelike nature can be accomplished by postselecting readings of the system's output according to the detector's reading. Experimentally, we measure the correlation between the current fluctuations in drains D2 (system) and D4 (detector) (*19*, *20*, *23*, *30*), which is proportional to the reduced joint-probability for simultaneously detecting electrons at the two drains

$$P(\delta\mathrm{D2} \times \delta\mathrm{D4}) = \frac{1}{4}\cos\left(\phi_S + \frac{\gamma}{2}\right)\cos\left(\phi_D + \frac{\gamma}{2}\right)\sin^2\left(\frac{\gamma}{2}\right) \qquad (3)$$

Note that the joint probability $P(\delta D2 \times \delta D4)$ is symmetric with regard to system and detector, which stresses the arbitrariness of their labeling. The expected visibility of the AB oscillation in the reduced joint probability is $v_{\mathrm{D2D4}} = \sin\left(\frac{\gamma}{2}\right)\cos\left(\phi_D + \frac{\gamma}{2}\right)$, which also obeys a complementarity relation with the which-path knowledge: ${v_{\mathrm{D2D4}}}^2 + K^2 = D^2$ (*18*).

We realized the system-detector complex in a two-dimensional electron gas (2DEG) embedded in a GaAs-AlGaAs heterostructure. A quantizing magnetic field (B = 4.4 T) put the 2DEG in the second filling factor of the quantum Hall effect, with a base temperature of 12 mK and an electron temperature of ~30 mK. Only the outer chiral edge channels (the lowest spin split Landau level) participated in the interference and the interaction, whereas the inner edge channels were fully reflected at QPC0, which precede QPC1 of both MZIs and, thus, played no active role. The outer edge channel, emanating from source contact S1 (S3), was split at SQPC1 (DQPC1) into two paths that subsequently interfered at SQPC2 (DQPC2). The AB phase is controlled by changing the area enclosed between the interfering paths via the system's modulation gate SMG (detector's DMG). The second filling factor was chosen because the devices were more stable and the visibility of the AB oscillation was reasonably high under these conditions; however, the two interacting paths were partly screened by the adjacent unbiased inner channels, which weakened the mutual interaction. The system's output current $\langle I_{D2}\rangle$ ($\langle I_{D4}\rangle$), measured in drain contact D2 (D4), was proportional to the phase-dependent transmission probability P(D2) [P(D4)]. For half transmission of QPC1 and QPC2, $|t_1|^2 = |t_2|^2 = \frac{1}{2}$, the visibility reached $\xi = 0.66$ in each MZI. Interaction between system and detector via the interacting paths, counterpropagating along 6 μm and separated by less than 2 μm, was controlled by surface gates, while avoiding tunneling between the interacting paths.

Under these conditions, the system's differential visibility v_{D2} was measured as a function of the detector's source current I_{S3} (Fig. 2). The visibility v_{D2} decreased by some 15% when

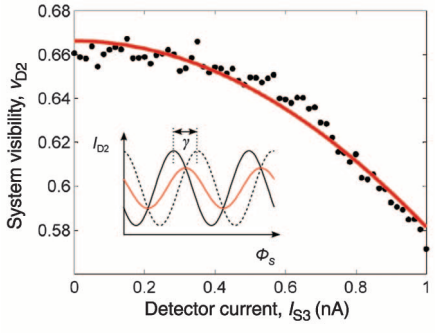

Fig. 2. Dephasing of the system by entanglement with the detector. The system visibility is reduced as the detector current is increased (dots). Red solid line: fit to Eq. 1 yielding $\xi = 0.66$ and $\gamma = \pi/6$ at I_{S3} = 1 nA. (**Inset**) Schematic representation of the AB-dependent current at D2, shown separately for electrons that did (dashed black line) and did not (solid black line) receive a "γ shift." The average of the two (red line) has AB oscillations with the same periodicity but reduced amplitude (partial dephasing).

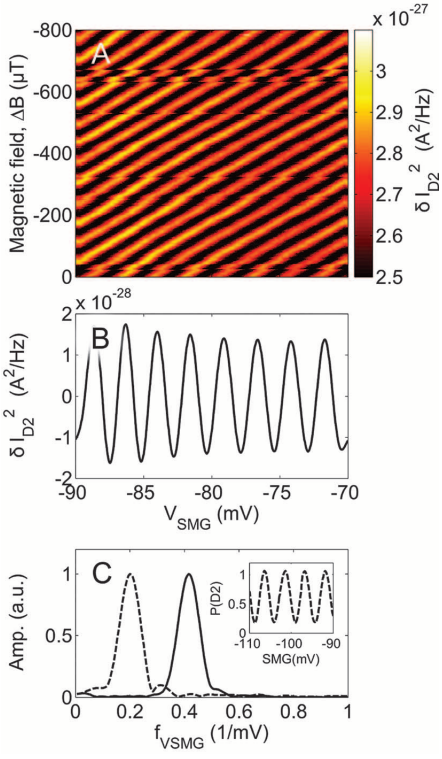

Fig. 3. AB dependence of the autocorrelation in the system. (**A**) The system's autocorrelation was measured while letting the magnetic field decay slowly (ΔB) and varying the system's area with the modulation gate (SMG) faster. (**B**) The average autocorrelation signal oscillates at half the periodicity of the AB oscillation in conductance, as seen in (**C**) discrete Fourier transforms of the AB oscillations in conductance (dashed line, 0.2 mV^{-1}) and in autocorrelation (full line, 0.4 mV^{-1}). (Inset) AB oscillations in conductance.

increasing the input current to 1 nA. This can be understood in two ways: (i) With the increased current, more electrons pass at any time through the interacting path of the detector, which increases the total phase shift a system electron undergoes and consequently the acquired which-path information, and (ii) in terms of interaction, potential fluctuations in the detector's interacting path increase with current, which leads to stronger dephasing of the system. If one assumes a linear dependence of γ on I_{S3}, the data fit theory with $\gamma \approx \pi/6$ at I_{S3} = 1 nA (Fig. 2, red line). Although dephasing due to power dissipation could also take place, it would not affect our main results; thermally induced dephasing is irreversible and, as such, cannot contribute to phase recovery by quantum erasure. Moreover, the consistence between the above value for γ and that obtained from the cross-correlation data (see below) suggests that dephasing due to power dissipation is minor. Also, note that the transmission of DQPC2 was varied and was found to have no effect on the dephasing of the system.

After quantifying the strength of interaction, equal source currents I_S = 0.5 nA were fed into both MZIs. The interacting paths were set to obtain maximal interaction, void of interchannel tunneling. Three zero-frequency correlation signals were measured simultaneously: (i and ii) autocorrelation of each drain current, $\langle \delta I_{D2}{}^2 \rangle$ and $\langle \delta I_{D4}{}^2 \rangle$, and (iii) cross-correlation of the two drain currents $\langle \delta I_{D2} \delta I_{D4} \rangle$. All three were measured as a function of SMG, which affected the system's phase ϕ_S, and the decaying magnetic field, which affected both ϕ_S and ϕ_D.

The autocorrelation of each interferometer is proportional to its shot noise. In the case of the system

$$\langle \delta I_{D2}{}^2 \rangle \propto S_{MZI} = 2eI_{S1}P(\mathrm{D2})[1 - P(\mathrm{D2})] = \frac{1}{4}eI_{S1}[1 - \cos(2\phi_S)] \quad (4)$$

where $P(D2)$ is the average transmission of the system. The shot noise oscillated at half the periodicity of the conductance (Fig. 3, B and C). The color plot in Fig. 3A was obtained by letting the magnetic field decay slowly while the voltage of SMG was scanned faster. Note that the magnitude of the shot noise in each MZI was considerably larger than predicted by Eq. 4, a phenomenon that was previously observed (*23*). Although this phenomenon remains unexplained, it could result from unobservable high-frequency charge fluctuations, which cause fluctuations in the AB phase that lower the visibility right from the start, as they are down-converted to the measured frequency by the partitioning of QPC2.

Our main result lies in the AB dependence of the zero-frequency cross-correlation between current fluctuations in D2 and D4, $\langle \delta I_{D2} \delta I_{D4} \rangle$ (Fig. 4A). The cross-correlation signal, merely 4×10^{-30} A^2/Hz, was extracted by a digital band-pass filter and compensated for the unavoidable magnetic field dependence of the system's interference pattern.

It may be easier to understand the cross-correlation color plot with two cuts at specific magnetic fields (Fig. 4B): One cut at ΔB = 103 μT (relative to B = 4.4 T), with rather strong oscillations in the cross-correlation as a function of V_{SMG}, and another at ΔB = 140 μT, with reduced cross-correlation oscillations. The AB oscillations in the cross-correlation retrace qualitatively the lost interference; the dependence of the cross-correlation visibility on ΔB is plotted in Fig. 4C.

The amplitude of the "checkerboard" pattern, observed in Fig. 4A, drops as γ^2 when the interaction is reduced (Eq. 3, $\gamma << \pi$). Therefore, as the interacting edges were separated, the distinctive checkerboard pattern vanished altogether (fig. S1); future works should be able to see the gradual quenching of the pattern as the interacting edges are carefully brought apart. This behavior is consistent with the system-detector's mutual interaction acting as the dominant source for the observed results.

In a more quantitative fashion, we compared the visibility of the cross-correlation oscillation (a wavelike property) with the which-path knowledge K (a particle-like property), which is obtained by an approximation of Eq. 2: for $\gamma << \pi, K(\phi_D) \propto |\gamma \frac{dI_{D4}}{d\phi_D}|$. Although being available from the AB conductance oscillation in the detector, we obtained the above derivative from the autocorrelation signal $\langle \delta I_{D4}{}^2 \rangle$, which was measured simultaneously with the cross-correlation signal. Plotting the cross-correlation visibility (Fig. 4C) and the knowledge, K (Fig. 4D), their anticorrelated dependence on ΔB is evident. The small shift between the two dependencies is attributed to the finite γ, which we estimate from the shift to be $\gamma \approx \pi/12$ for I_{S3} = 0.5 nA; this is consistent with the previously found $\gamma \approx \pi/6$ for I_{S3} = 1 nA. The oscillations in the cross-correlation visibility are larger than the expected $\sin^2(\gamma/2) = 0.017$ (Eq. 3), similar to the excess noise in the autocorrelation. The anticorrelation between the cross-correlation visibility and the which-path knowledge demonstrates that erasing which-path information allows recovery of the system's wavelike nature.

Two major differences between electrons and photons, which are customarily used in this type of experiments, are their exchange statistics and strong coulomb interaction. The former allows a highly controlled autocorrelation and noise-free current, because of Pauli's exclusion principle; the latter makes the electrons vulnerable to dephasing but, at the same time, allows control of the entanglement strength and phase manipulation. Our work can be expanded upon by realizing a delayed choice (*31*) or a spin-entangled device (*32*), or a three-electron–entangled (GHZ) state (*33*). Moreover, the electronic quantum eraser could be used to measure weak values (*34*) or the Bell inequality (*35*) for the entangled electrons.

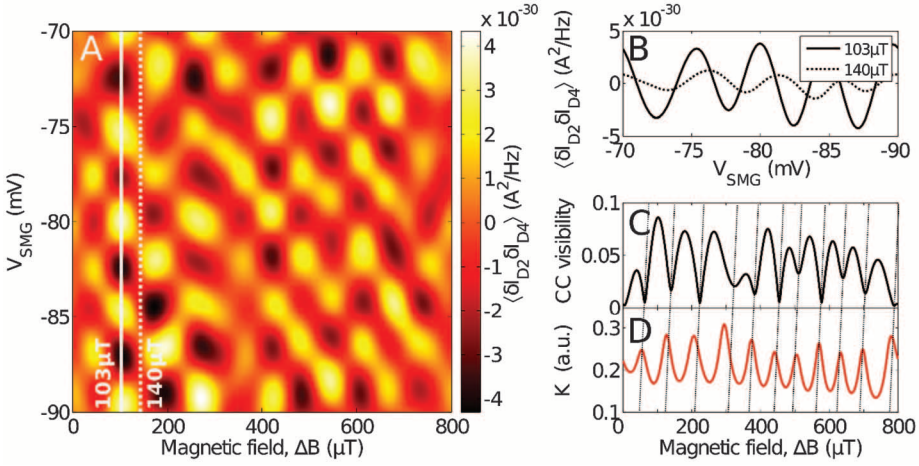

Fig. 4. Phase recovery by quantum erasure. (**A**) The cross-correlation of the system and detector output currents. (**B**) Cuts of the color plot in (A) for two values of the magnetic field, as marked in (A). There is near anticorrelation between (**C**) the oscillation visibility and (**D**) the which-path knowledge, which shows that quantum erasure allows the recovery of interference; the dashed lines serve as guides to the eye. The slight shift from perfect anticorrelation allows us to estimate $\gamma \approx \pi/12$ for I_{S3} = 0.5 nA.

REFERENCES AND NOTES

1. N. Bohr, *Nature* **121**, 580–590 (1928).
2. R. Feynman, R. Leighton, M. Sands, *The Feynman Lectures on Physics*, vol. 3, *Quantum Mechanics* (Addison-Wesley, Reading, MA, 1965).
3. M. O. Scully, B. G. Englert, H. Walther, *Nature* **351**, 111–116 (1991).
4. B. G. Englert, M. O. Scully, H. Walther, *Nature* **375**, 367–368 (1995).
5. E. P. Storey, S. M. Tan, M. J. Collett, D. F. Walls, *Nature* **375**, 368–368 (1995).
6. D. I. Chang *et al.*, *Nat. Phys.* **4**, 205–209 (2008).
7. S. Dürr, T. Nonn, G. Rempe, *Nature* **395**, 33–37 (1998).
8. P. Bertet *et al.*, *Nature* **411**, 166–170 (2001).
9. M. O. Scully, K. Drühl, *Phys. Rev. A* **25**, 2208–2213 (1982).
10. P. G. Kwiat, A. M. Steinberg, R. Y. Chiao, *Phys. Rev. A* **45**, 7729–7739 (1992).
11. T. J. Herzog, P. G. Kwiat, H. Weinfurter, A. Zeilinger, *Phys. Rev. Lett.* **75**, 3034–3037 (1995).
12. P. G. Kwiat, A. M. Steinberg, R. Y. Chiao, *Phys. Rev. A* **49**, 61–68 (1994).
13. Y. H. Kim, R. Yu, S. P. Kulik, Y. Shih, M. O. Scully, *Phys. Rev. Lett.* **84**, 1–5 (2000).
14. X. S. Ma *et al.*, *Proc. Natl. Acad. Sci. U.S.A.* **110**, 1221–1226 (2013).
15. A. Peruzzo, P. Shadbolt, N. Brunner, S. Popescu, J. L. O'Brien, *Science* **338**, 634–637 (2012).
16. F. Kaiser, T. Coudreau, P. Milman, D. B. Ostrowsky, S. Tanzilli, *Science* **338**, 637–640 (2012).
17. Y. Ji *et al.*, *Nature* **422**, 415–418 (2003).
18. K. Kang, *Phys. Rev. B* **75**, 125326 (2007).

19. J. Dressel, Y. Choi, A. N. Jordan, *Phys. Rev. B* **85**, 045320 (2012).
20. F. Buscemi, P. Bordone, A. Bertoni, *Eur. Phys. J. D* **66**, 312–323 (2012).
21. E. Buks, R. Schuster, M. Heiblum, D. Mahalu, V. Umansky, *Nature* **391**, 871–874 (1998).
22. D. Sprinzak, E. Buks, M. Heiblum, H. Shtrikman, *Phys. Rev. Lett.* **84**, 5820–5823 (2000).
23. I. Neder, M. Heiblum, D. Mahalu, V. Umansky, *Phys. Rev. Lett.* **98**, 036803 (2007).
24. Y. Aharonov, D. Bohm, *Phys. Rev.* **115**, 485–491 (1959).
25. B. Rosenow, Y. Gefen, *Phys. Rev. Lett.* **108**, 256805 (2012).
26. A. Stern, Y. Aharonov, Y. Imry, *Phys. Rev. A* **41**, 3436–3448 (1990).
27. W. K. Wootters, W. H. Zurek, *Phys. Rev. D Part. Fields* **19**, 473–484 (1979).
28. G. Jaeger, A. Shimony, L. Vaidman, *Phys. Rev. A* **51**, 54–67 (1995).
29. B. G. Englert, *Phys. Rev. Lett.* **77**, 2154–2157 (1996).
30. I. Neder *et al.*, *Nature* **448**, 333–337 (2007).
31. J. Wheeler, W. Zurek, *Quantum Theory and Measurement* (Princeton Univ. Press, Princeton, NJ, 1983).
32. W. Chen *et al.*, *Phys. Rev. B* **87**, 155308 (2013).
33. A. A. Vyshnevyy, G. B. Lesovik, T. Jonckheere, T. Martin, *Phys. Rev. B* **87**, 165417 (2013).
34. V. Shpitalnik, Y. Gefen, A. Romito, *Phys. Rev. Lett.* **101**, 226802 (2008).
35. A. A. Vyshnevyy, A. V. Lebedev, G. B. Lesovik, G. Blatter, *Phys. Rev. B* **87**, 165302 (2013).

ACKNOWLEDGMENTS

We thank K. Kang, Y. Chung, I. Neder, and H. Inoue for useful discussions. M.H. and Y.G. acknowledge the partial support of the Israeli Science Foundation, the Minerva foundation, and the U.S.-Israel Binational Science Foundation (BSF). M.H. acknowledges also the support of the European Research Council under the European Community's Seventh Framework Program (FP7/2007-2013)/ERC grant agreement no. 227716, and the German Israeli Project Cooperation (DIP).

SUPPLEMENTARY MATERIALS

www.sciencemag.org/content/344/6190/1363/suppl/DC1
Materials and Methods
Supplementary Text
Figs. S1 to S3
References (*36*, *37*)

13 November 2013; accepted 23 May 2014
10.1126/science.1248459

NANOMAGNETISM

Nanoscale imaging and control of domain-wall hopping with a nitrogen-vacancy center microscope

J.-P. Tetienne,[1,2] T. Hingant,[1,2] J.-V. Kim,[3] L. Herrera Diez,[3] J.-P. Adam,[3] K. Garcia,[3] J.-F. Roch,[1] S. Rohart,[4] A. Thiaville,[4] D. Ravelosona,[3] V. Jacques[1,2]*

The control of domain walls in magnetic wires underpins an emerging class of spintronic devices. Propagation of these walls in imperfect media requires defects that pin them to be characterized on the nanoscale. Using a magnetic microscope based on a single nitrogen-vacancy (NV) center in diamond, we report domain-wall imaging on a 1-nanometer-thick ferromagnetic nanowire and directly observe Barkhausen jumps between two pinning sites spaced 50 nanometers apart. We further demonstrate in situ laser control of these jumps, which allows us to drag the domain wall along the wire and map the pinning landscape. Our work demonstrates the potential of NV microscopy to study magnetic nano-objects in complex media, whereas controlling domain walls with laser light may find an application in spintronic devices.

Magnetic domain walls (DWs) represent nanoscale objects that form the cornerstone of a number of emerging spintronic applications, such as the racetrack memory (*1*), the magnetic random access memory (*2*), or the magnetic memristor (*3*). In such schemes, precise control of the positioning and motion of a single DW or a sequence of DWs along a track is paramount for their operation (*4*). However, in materials important for technology, such as ultrathin films with perpendicular magnetic anisotropy (*5*), defects can result in considerable pinning that impedes wall propagation. This pinning effect has two important consequences. First, it introduces a stochastic component into the wall dynamics, whereby thermally driven processes involving hopping over energy barriers, or Barkhausen jumps, become important. Second, these processes can involve deformations in the DW profile itself, resulting in more complex two-dimensional (2D) dynamics such as creep in the low-velocity regime (*6*, *7*). It is therefore an important challenge to quantify these aspects experimentally for realistic sample geometries.

The capacity to directly image DWs in nanostructures would provide valuable insight into how the structure of a DW deforms as it navigates through a complex energy landscape shaped by a random network of material defects. However, experimental techniques that allow this for practical spintronic devices with the requisite nanoscale spatial resolution are scarce. Techniques based on x-ray (*8*) or electron (*9*) microscopy, for example, suffer from a lack of signal because of the small interaction volumes in nanometer-thick films, whereas magnetic force microscopy is usually not suitable because DWs in ultrathin films are highly sensitive to magnetic perturbations. Other techniques, such as spin-polarized scanning tunneling microscopy (*10*) and spin-polarized low-energy electron microscopy (*11*), can provide sufficient resolution to image wall structures but are limited to model systems.

Over the past few years, scanning nitrogen-vacancy (NV) center microscopy has emerged as a powerful magnetic imaging technique that provides quantitative measurements of the stray magnetic field emanating from a micromagnetic structure (*12*–*16*). This method is highly sensitive (*17*), produces no detectable magnetic backaction on the sample, and allows for a spatial resolution ultimately limited by the atomic size of the probe. This technique recently enabled stray-field imaging of a single electron spin (*18*) and of the vortex core in a magnetic microdot (*19*, *20*). Here, we use scanning NV center microscopy to image, study, and control DWs in perpendicularly magnetized ultrathin wires.

The scanning NV center microscope employs the electronic spin of a single NV defect hosted in a diamond nanocrystal, which is attached to the tip of an atomic force microscope (*21*) and used as a magnetic field sensor (Fig. 1A). The magnetic field is evaluated within an atomic-size detection volume by encoding Zeeman shifts of the electron spin sublevels onto the spin-dependent photoluminescence (PL) intensity of the NV defect (*16*). To this end, a laser beam at the wavelength $\lambda = 532$ nm is tightly focused onto the NV defect with a high–numerical aperture microscope objective, whereas a radiofrequency source allows for manipulation of its electron spin state. The spin-dependent red PL intensity of the NV defect is collected by the same objective and forms the magnetometer signal, which gives information about the projection $|B_{NV}|$ of the local magnetic field along the NV center's quantization axis u_{NV} (Fig. 1A) (*19*, *22*).

We studied a 1.5-μm-wide Ta/CoFeB(1 nm)/MgO wire that exhibits perpendicular magnetic anisotropy (Fig. 1B). After preparing well-isolated DWs by applying short magnetic field pulses (*22*), the stray magnetic field was measured while operating the scanning NV center microscope in the "dual iso-B" imaging mode, which provides two different iso–magnetic field (iso-B) contours (*19*, *21*). Figure 1C shows a typical magnetic field map

[1]Laboratoire Aimé Cotton, CNRS, Université Paris-Sud and ENS Cachan, UPR CNRS 3321, 91405 Orsay, France.
[2]Laboratoire de Photonique Quantique et Moléculaire, ENS Cachan and CNRS, UMR CNRS 8537, 94235 Cachan, France.
[3]Institut d'Electronique Fondamentale, Université Paris-Sud and CNRS, UMR CNRS 8622, 91405 Orsay, France.
[4]Laboratoire de Physique des Solides, Université Paris-Sud and CNRS, UMR CNRS 8502, 91405 Orsay, France.
***Corresponding author. E-mail: vjacques@ens-cachan.fr**